Dual-Stage Nanopositioning for High-Speed Scanning Probe Microscopy

Tomas Tuma, *Member, IEEE*, Walter Haeberle, Hugo Rothuizen, *Member, IEEE*, John Lygeros, *Fellow, IEEE*, Angeliki Pantazi, *Member, IEEE*, and Abu Sebastian, *Senior Member, IEEE*

***Abstract*—This paper presents a dual-stage approach to nanopositioning in which the tradeoff between the scanner speed and range is addressed by combining a slow, large-range scanner with a short-range scanner optimized for high-speed, high-resolution positioning. We present the design, finite-element simulations, and experimental characterization of a fast custom-built short-range scanner. The short-range scanner is based on electromagnetic actuation to provide high linearity, has a clean, high-bandwidth dynamical response and is equipped with a low-noise magnetoresistance-based sensor. By using advanced noise-resilient feedback controllers, the dual-stage system allows large-range positioning with subnanometer closed-loop resolution over a wide bandwidth. Experimental results are presented in which the dual-stage scanner system is used for imaging in a custom-built atomic force microscope.**

***Index Terms*—Atomic force microscopy (AFM), control design, mechatronics, nanopositioning.**

I. Introduction

PRECISE positioning on the nanometer scale, often referred to as *nanopositioning*, is a key enabling technology for nanoscale science and engineering. With a vast range of applications across various fields such as information technology [1], semiconductor manufacturing [2], and biology [3], nanopositioning has become an important interdisciplinary research topic interconnecting the fields of control, mechanical, and electrical engineering.

One of the key techniques in nanotechnology that critically relies on nanopositioning is scanning probe microscopy (SPM) [4]. SPM allows the interrogation and interaction with matter down to the atomic level by probing surfaces with an atomically sharp probe tip. For instance, in atomic force microscopy (AFM), which is a type of SPM, the probe is positioned relative to the sample by means of a nanopositioner (often called a *scanner*), and the properties of the sample surface are inferred from the forces acting on the probe tip as it traverses the sample.

Manuscript received November 18, 2012; revised March 15, 2013; accepted May 7, 2013. Date of publication June 26, 2013; date of current version April 11, 2014. Recommended by Technical Editor Y. Sun.

T. Tuma is with IBM Research—Zurich, 8803 Rueschlikon, Switzerland, and also with the Automatic Control Laboratory, Swiss Federal Institute of Technology, 8092 Zurich, Switzerland (e-mail: uma@zurich.ibm.com).

W. Haeberle, H. Rothuizen, A. Pantazi, and A. Sebastian are with IBM Research—Zurich, 8803 Rueschlikon, Switzerland (e-mail: wha@zurich.ibm.com; rth@zurich.ibm.com; agp@zurich.ibm.com; ase@zurich.ibm.com)

J. Lygeros is with the Automatic Control Laboratory, Swiss Federal Institute of Technology, 8092 Zurich, Switzerland (e-mail: lygeros@control.ee.ethz.ch).

Color versions of one or more of the figures in this paper are available online at http://ieeexplore.ieee.org.

Digital Object Identifier 10.1109/TMECH.2013.2266481

Significant research efforts have been devoted to the design and control of SPM scanners [5]. Piezoelectric tube scanners were first introduced for scanning tunneling microscopy in 1986 [6] and have been used extensively in SPM [7]–[9] owing to their high resolution and low cost. Their disadvantage is the low resonant frequencies and a relatively large amount of cross coupling. In another approach, piezo-actuated flexure-guided scanners with serial or parallel kinematics are used, which can reach a high actuation bandwidth and at the same time, retain excellent mechanical properties [10]–[13].

To achieve high positioning precision over a high bandwidth, SPM scanners are typically operated under feedback control. Feedback control is essential to compensate for environmental disturbances such as building vibrations and temperature fluctuations, and also for fabrication uncertainties, mechanical resonances, and nonlinearities of the actuator. The closed-loop resolution, determined by the closed-loop bandwidth and the sensor characteristics, is of critical importance as it governs the overall resolution of the SPM. In high-speed SPM, the closed-loop bandwidth is typically large which leads to an increase in the amount of measurement noise that enters the feedback loop and deteriorates the resolution. Even if high-end noncontact sensors are used for position feedback, the standard deviation of the position measurement signal amounts to several nanometers over the closed-loop bandwidth.

This paper presents the design and characterization of a dual-stage nanopositioning system specifically tailored for high-resolution subnanometer positioning at high speeds. To that end, the nanopositioning system is designed to meet three fundamental requirements. First, a high open-loop bandwidth is required to enable both high-speed and high-resolution operation. Allowing low open-loop bandwidth would deteriorate the closed-loop resolution as a broadband control effort would be required to obtain a flat closed-loop frequency response over a wide bandwidth. Second, well-defined dynamics and high linearity are required, such that the scanner can be modeled accurately and used with advanced noise-resilient feedback controllers, such as resonant control [14], feedback controllers with a shaped noise-sensitivity transfer function [15], signal transformation [16] and impulsive control [17]. Third, a large scan range is required; the bandwidth and linearity should not be obtained at the expense of the scan range.

Conventional SPM scanners based on the piezoelectric actuation principle, such as piezoelectric tube scanners and piezo-actuated flexure stages, do not satisfy the aforementioned requirements owing to the inherent nonlinear characteristics of piezoelectric actuators, such as drift, creep, and hysteresis [18].

To compensate for these nonlinearities, feedback control over a wide bandwidth is typically required, which negatively affects the positioning resolution. To circumvent these problems, our scanner design is based on electromagnetic actuation which has been widely used in applications such as in hard-disk magnetic recording [19], probe-based data storage [20], [21] tape storage [22], and semiconductor lithography [23]. The advantage of electromagnetic actuation is its high linearity; on the other hand, electromagnetic actuators typically provide only limited actuation force, which has to be reflected in the scanner design.

To illustrate a fundamental tradeoff involved in the scanner design, let us assume that the dynamical response of the scanner resonant modes can be modeled as that of a harmonic oscillator. A simple harmonic oscillator with mass m and stiffness k has the resonant frequency

$$\omega = \sqrt{\frac{k}{m}}. \tag{1}$$

Hence, to obtain a high open-loop bandwidth, the mass of the scanner should be minimized and the stiffness maximized. However, the extent to which the mass can be minimized is limited because of the manufacturing process as well as the ability to mount samples with variable mass. On the other hand, increasing the stiffness of the scanner conflicts with achieving large scan ranges with the limited actuation force of the electromagnetic actuator. This is a fundamental design tradeoff which renders the aforementioned requirements challenging if not impossible to achieve in a conventional scanner design.

This paper presents a novel approach based on decoupling the requirements on the speed and the range of the scanner, an idea central to the dual-stage positioning concept as known, for example, in the field of optical recording [24], hard-disk magnetic recording [25], robotics [26], [27], and micromanipulation [28]. In SPM, the dual-stage concept was introduced in vertical positioning [29], [30], but so far, only little research effort has been devoted toward dual-stage lateral nanopositioning.

In the dual-stage nanopositioning system introduced in this paper, two serially coupled scanners are used: a first-stage scanner for large-range positioning with a low bandwidth (*large-range scanner*) and a second-stage scanner for short-range positioning with a high bandwidth (*short-range scanner*). The large-range scanner is a commercial piezo-actuated stage with three-degrees-of-freedom displacement capability, whereas the electromagnetically actuated short-range scanner is custom-designed for high-speed operation along a single axis. This configuration is particularly suitable for the widely used raster-scanning SPM, but can also be used for more recent scanning modes such as feature tracking [31]. The prototype system demonstrated in this paper achieves real-time video-rate SPM imaging with nanometer-scale resolution and speed of more than 1 frame/s, while having a range of 100 μm which is above most state-of-the-art SPM flexure-based nanopositioners (a recent comparison can be found e.g. in [12]). This study is based on the preliminary results published in [32] and [33].

This paper is organized as follows. In Section II, we present the mechanical design, finite-element simulations, and modeling of the custom-designed short-range scanner. In Section III, the experimental characterization of the scanner is presented, including measurements of the scanner range, dynamic response and thermomechanical coupling. Section IV presents a noise-resilient feedback control design for the short-range scanner. Section V presents experimental results in which the dual-stage system is used for high-speed and large-range imaging in a custom-built AFM. Section VI concludes the paper.

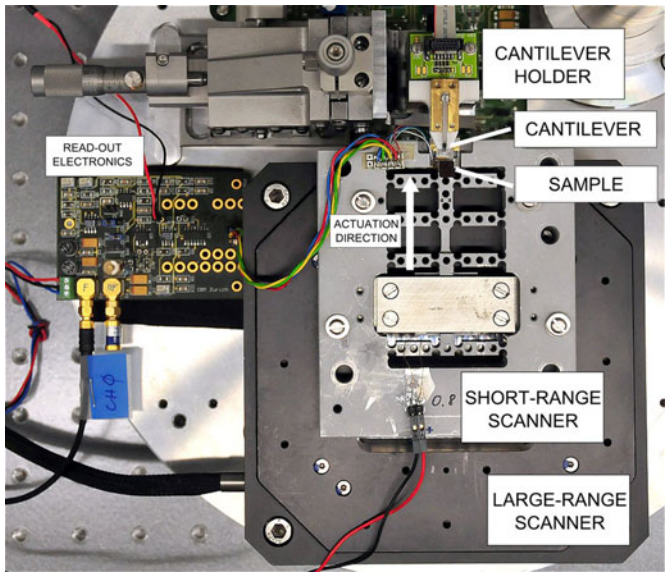

Fig. 1. Photograph of the dual-stage scanner system, showing the single-axis short-range scanner mounted on the three-axis large-range positioning stage.

II. Scanner Design

Because most nanopositioning applications are of the raster-scan type, the more demanding tradeoffs between positioning range, bandwidth, and accuracy apply to only one axis. By using a custom-built short-range scanner, our dual-stage approach improves the performance, for this one axis, in the high-frequency portion of the dynamic range, while retaining the larger stroke of the slower in-plane axis. Fig. 1 shows a photograph of the overall prototype scanner system. Slow, large-range positioning for all axes is provided by a commercial three-axis piezo-actuated positioner (model PI-517 from Physik Instrumente), with stroke ranges of 100 μm for the in-plane directions x and y, and 20 μm for z out-of plane. The custom-built short-range scanner is mounted directly on the large-range scanner and is specifically designed for high speed, high linearity, and clean dynamical behavior in the fast positioning axis. In the following, the mechanical design of the short-range scanner is described in detail, along with a model of the dynamics in the actuation direction and a built-in high-bandwidth position sensor.

A. Design Considerations

The custom-built short-range scanner for high-speed positioning comprises two rigidly linked moving bodies, a sample-carrying table, and an actuator subassembly, each of which is guided uniaxially by a set of profiled flexures. A cross-sectional schematic of the short-range scanner, including actuation and

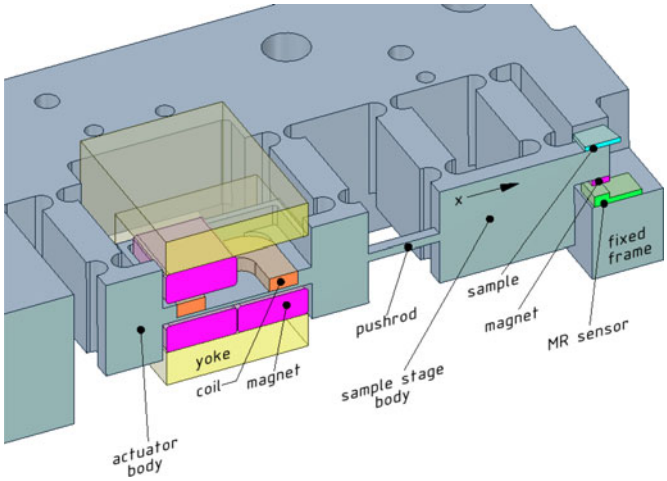

Fig. 2. Half-symmetry crosssection of the short-range scanner. The lightening holes and one of the magnets have been omitted in this view for clarity.

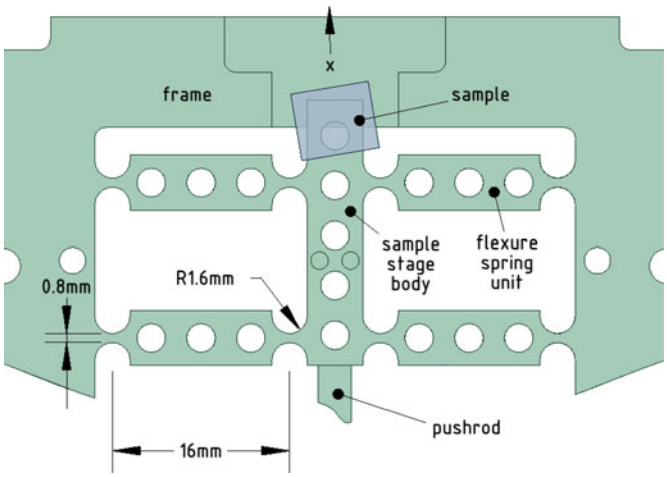

Fig. 3. Detail of the scan table subassembly and the suspension springs of the short-range scanner.

position sensing components discussed in Section II-D, is shown in Fig. 2.

The suspension of each of the moving parts is based on four high-aspect-ratio flexure spring units arranged in symmetrical pairs on either side of the moving bodies, as shown in a cut-away view in Fig. 3. Each flexure unit is shaped with two circular notch hinges for a well-controlled location of bending and ease of fabrication. Having found single-side suspension inadequate in preliminary simulations, due to excessive run out and compliance in the out-of-plane direction, we opted for this doubly clamped configuration which provides much better cross-talk performance [12], [34]. Although the doubly clamped boundary conditions do lead to stress-stiffening in principle, the relative length of the flexures (16 mm between the circular notch hinges) compared to the small displacement range required (on the order of ± 1 μm) makes these nonlinearities negligible.

We use electromagnetic actuation over the more conventional choice of a piezo stack in order to ensure linearity, and in particular to avoid the latter's hysteretic behavior. The actuator consists of a racetrack-shaped flat coil located on the rotor (moving) side, and an arrangement of four NdFeB magnets on the stator side, which immerse the long sides of the coil in a uniform magnetic field and generate Lorentz forces on the coil winds along the intended direction of motion (x). The measured force gain of this actuator is approximately 0.9 N/A. The actuator is driven by a low-noise voltage-to-current amplifier with gain of 0.08 A/V. In the control design and experiments presented in the remainder of this paper, the voltage-to-current amplifier is considered a part of the actuator for brevity.

Decoupling of the two moving bodies via the small-section (1.2 mm $\times$ 3.0 mm) connection rod serves two purposes: first, to mechanically attenuate the effects of any residual out-of-plane forces exercised by the actuator on the sample table, and secondly, to lengthen the thermal time constant of heat-up of the sample table subassembly when the actuator is run at high power or low-duty cycle. Lastly, we have perforated all moving parts with lightening holes in order to decrease the carried mass, and thereby make the stage faster.

B. Finite-Element Simulations

A summary of the eigenmode shapes obtained in a modal analysis using the commercial tool for finite-element analysis ANSYS is shown in Fig. 4. The principle eigenmodes of interest are the fundamental modes of the suspension system, corresponding to intended actuation along the fast axis, and mode 5, which corresponds to the elongation/compression of the connection rod along its long axis due to finite material stiffness. Other eigenmodes in the intermediate frequency range involve bending of the coil-holding frame, and are not expected to show up in a significant way in the dynamics unless the actuation components are misaligned so as to generate a significant out-of-plane force or bending moment.

C. Model

The short-range scanner was specifically designed with the objective of clean dynamical behavior over the whole actuation bandwidth in order to simplify the design, modeling, and feedback control of the scanner. To that end, the scanner was designed such that its dynamics in the actuation direction correspond to an interconnection of harmonic oscillators.

The dynamics in the actuation direction can be accurately modeled as a spring-mass-damper system with two masses connected by spring-damper pairs as shown in the free-body diagram in Fig. 5. The masses m_a and m_s correspond to the actuator body and the scan table body, respectively. These two masses are connected by the small-section connection rod which is modeled as a spring-damper system with stiffness k_r and damping coefficient c_r, respectively, to capture effects related to its finite stiffness at high frequencies. The connection of the actuator and the scan table body to the mechanical ground is also modeled with spring-damper pairs with coefficients k_a and c_a for the actuator side and k_s and c_s for the scan table side, respectively.

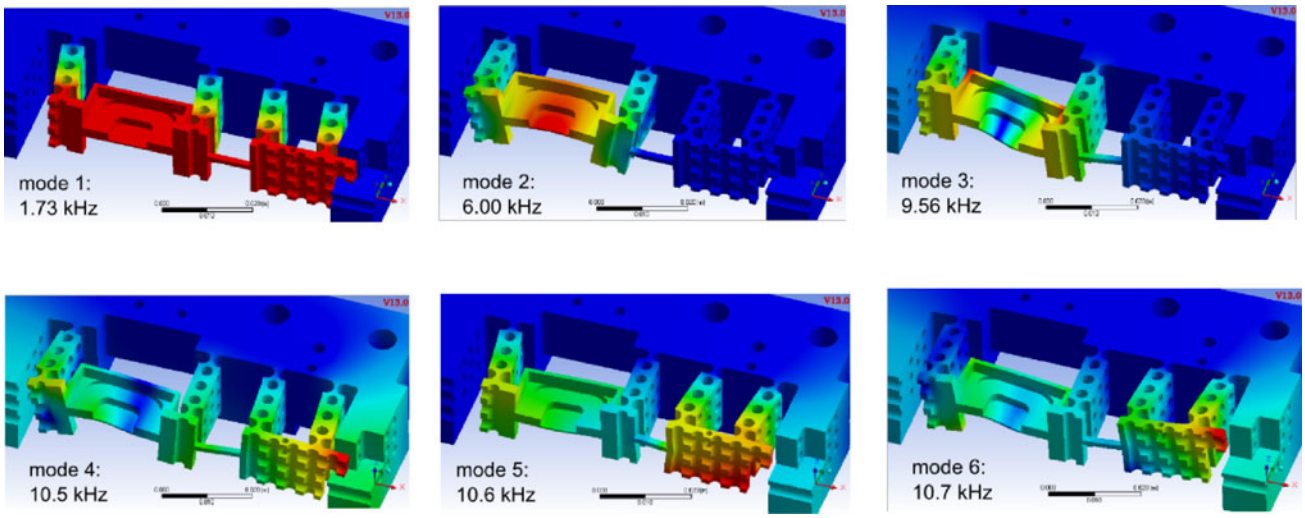

Fig. 4. Eigenmode shapes from finite-element modal analysis. Only the half-symmetry cross section is shown in the figure for illustration purposes, however, the simulation was done for the complete system.

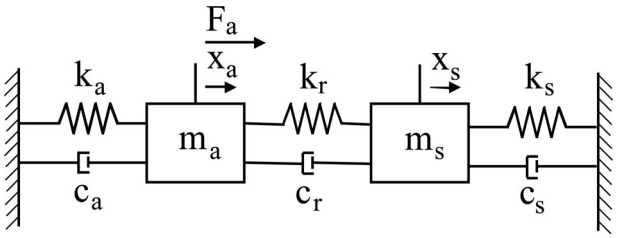

Fig. 5. Free-body diagram of a two-mass model of the short-range scanner.

TABLE I
COEFFICIENTS USED IN THE TWO-MASS MODEL OF THE SHORT-RANGE SCANNER

Actuator		Scan table		Rod	
m_a (kg)	0.0126	m_s (kg)	0.002	k_r (N/m)	7×10^6
k_a (N/m)	10^6	k_s (N/m)	10^6	c_r	0.8
c_a	0.8	c_s	0.8		

By using Newton's laws of motion, the equations governing the scanner motion are

$$F_a(t) = m_a\ddot{x}_a(t) + k_a x_a(t) + c_a\dot{x}_a(t) + k_r(x_a(t) - x_s(t)) + c_r(\dot{x}_a(t) - \dot{x}_s(t)) \quad (2)$$

$$0 = m_s\ddot{x}_s(t) + k_s x_s(t) + c_s\dot{x}_s(t) + k_r(x_s(t) - x_a(t)) + c_r(\dot{x}_s(t) - \dot{x}_a(t)). \quad (3)$$

Here, x_a and x_s denote the position of the actuator and scan table body, respectively, and F_a specifies the actuation force exerted on the actuator body. Using the above equations, the motion of the scan table, $y(t)$, in response to the actuation, $u(t)$, can be modeled as the state-space system

$$\dot{x}(t) = Ax(t) + Bu(t)$$
$$y(t) = Cx(t) \quad (4)$$

with the four-component state

$$x(t) = [\,x_a(t) \quad \dot{x}_a(t) \quad x_s(t) \quad \dot{x}_s(t)\,] \quad (5)$$

the dynamics matrix

$$A = \begin{bmatrix} 0 & 1 & 0 & 0 \\ -\dfrac{k_a + k_r}{m_a} & -\dfrac{c_a + c_r}{m_a} & \dfrac{k_r}{m_a} & \dfrac{c_r}{m_a} \\ 0 & 0 & 0 & 1 \\ \dfrac{k_r}{m_s} & \dfrac{c_r}{m_s} & -\dfrac{k_r + k_s}{m_s} & -\dfrac{c_r + c_s}{m_s} \end{bmatrix} \quad (6)$$

the input matrix

$$B = [\,0 \quad 1/m_a \quad 0 \quad 0\,] \quad (7)$$

and the output matrix

$$C = [\,0 \quad 0 \quad 1 \quad 0\,]. \quad (8)$$

Fig. 6 compares the transfer function between the actuation force, $F_a(t)$, and the scan table displacement, $x_s(t)$, as calculated using the finite-element simulations and using the previous four-state state space model. As expected from the eigenmode analysis, the dynamics are very clean with just two dominant vibrations modes in the frequency region up to 10 kHz. The effective masses, spring and damping constants are shown in Table I. Despite its conceptual and computational simplicity, the two-mass model provides an accurate estimate of the scanner dynamics. Experimental results presented later show that

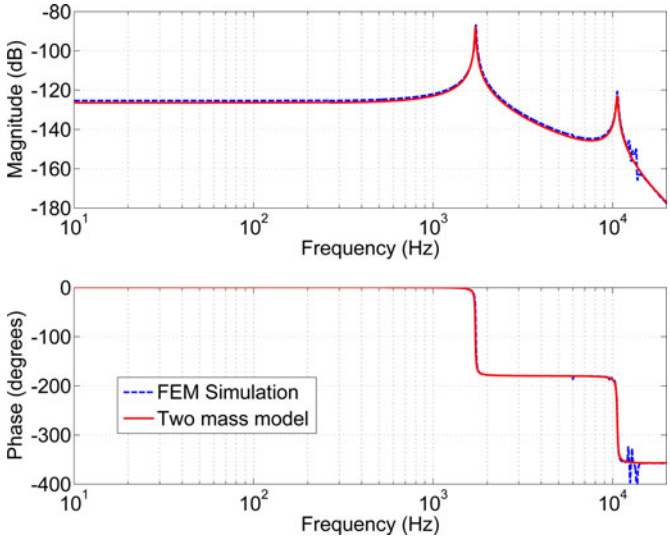

Fig. 6. Estimated frequency response between the actuation signal and the displacement of the scan table in the actuation direction. The figure compares the response obtained from finite-element simulation to that computed using the two-mass model.

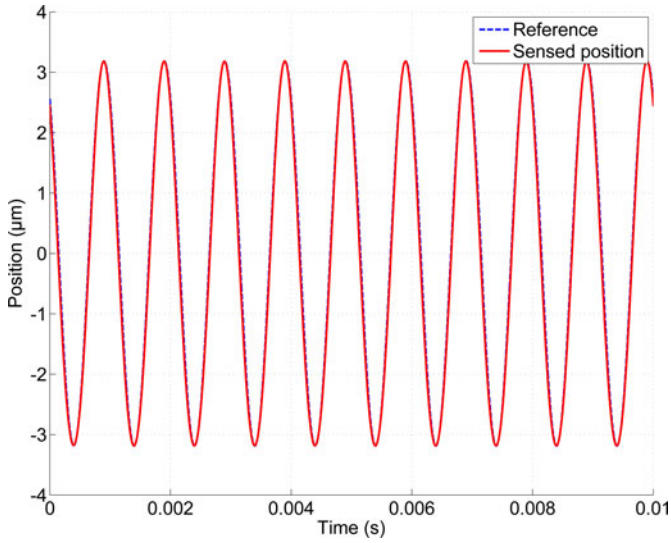

Fig. 7. Open-loop scan with frequency of 1000 Hz and range of 6 μm. The position was sensed using the GMR-based position sensor of the short-range scanner.

this estimate is also close to the real response of the scanner prototype.

D. Displacement Sensing

The short-range scanner is equipped with a highly sensitive displacement sensor based on the effect of giant magnetoresistivity (GMR) [13], [35] for position measurements along the actuation axis. We have chosen a GMR-based sensor because of its high bandwidth, low level of measurement noise, and small form factor. Besides meeting the aforementioned requirements on performance, GMR sensors have a low cost and require only simple read-out electronics.

The GMR sensing element used in the setup (NVE Corporation, Eden Prairie, MN, USA) has four sensing elements of size of approximately 40 $\times$ 100 μm connected in a Wheatstone bridge configuration. This configuration mitigates the effect of ambient temperature changes. The sensor is mounted on the stationary frame of the scanner under the scan table on which the sample is mounted. A permanent rare earth (NdFeB) magnet of size 1.2 mm $\times$ 2.7 mm $\times$ 0.8 mm is mounted on the scan table such that the magnetic field at the GMR sensor is modulated as the scan table moves. The magnet is oriented such that its magnetic moment is in a direction perpendicular to the sensor plane and to the sensing direction. The position of the GMR sensor was fine-tuned to maximize the magnetic field gradient in the sensing direction that is acting on the GMR sensing elements; the standard deviation of the sensor noise over the frequency range of 0 to 10 kHz is imately 0.7 nm. The nonlinearity of the sensor over the effective sensing range depends on the range of motion, targeted sensitivity, the characteristics of the sensing element, and the magnet geometry; the typical nonlinearity measured was below 0.2%. The sensor was calibrated against an externally-mounted optical measurement probe (MTI Instruments MTI-2100).

III. Experimental Characterization

In this section, experimental characterization of a prototype of the short-range scanner designed in Section II is presented. The prototype was fabricated from a monolithic aluminum block using standard CAM processes. The measurements of the open-loop scan range and linearity, dynamic response, and thermo-mechanical coupling measurements are presented.

A. Scan Range and Linearity

Fig. 7 shows an experimentally measured open-loop response of the scanner to a harmonic actuation signal of 1000 Hz frequency which results in the motion of approximately 6 μm peak-to-peak range. The corresponding gain of the actuator is approximately 7.5 μm/A. As expected from the electromagnetic actuator and the predicted dynamics of the scanner, the open-loop scanner response is highly linear (with nonlinearity of approximately 1.5% over the full scan range) and has a sufficient range for short-range operation in the dual-stage system.

B. Dynamic Response

The dynamics of the short-range scanner, predicted using finite-element simulations, are shown in Fig. 8 by a blue curve. The transfer function is computed between the applied actuator force (linear with drive current) and the displacement of the sample table. The frequency response of the fabricated prototype was obtained experimentally and is also shown in the figure, by a dashed red curve. There is a solid agreement between the dynamics as simulated and experimentally measured; the experimental results show a deviation in the first dominant resonant frequency of less than 1% with respect to the simulated results. This difference can occur due to uncertainties in the manufacturing process, variations in the materials used for fabrication, variations in the weight of the actuation components, and loading of the scan table, for example due to the sample weight.

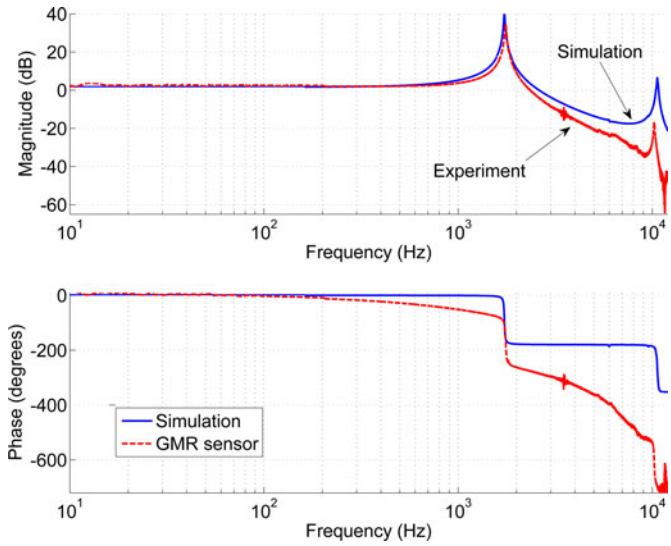

Fig. 8. Transfer function between the actuation signal and the scan table displacement in the actuation direction. The figure compares the frequency response obtained using finite-element simulations with the experimentally measured frequency response. The phase delay in the experimental measurement is due to the actuation amplifier.

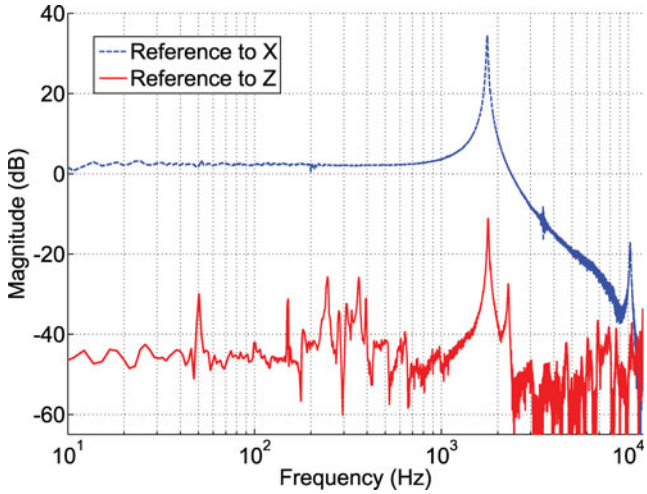

Fig. 9. Out-of-plane crosstalk measurement. The figure compares the experimentally obtained transfer function from the actuation signal to the displacement of the scan table in the actuation direction (denoted as X) with that to the out-of-plane scan table displacement (denoted as Z).

Also, the finite-element model does not account for dynamics of the actuation and sensing components, such as the actuator amplifier. A slight variation in the dynamics is inevitable and can be compensated by means of feedback control.

As mentioned earlier, the connecting rod helps with mechanically attenuating the effects of any residual out-of-plane forces exercised by the actuator on the scan-table. With this feature, the crosstalk to the y- and z-axis arising from the x motion is very low; the attenuation of more than 80 and 50 dB, respectively, is predicted in the simulations. The out-of-plane cross-talk which was expected to be more dominant owing to the construction of the scanner was measured experimentally by using an externally mounted photonic sensor (MTI Instruments MTI-2100). Fig. 9 compares the frequency response from the x actuation signal to the z motion signal with that to the intended x motion signal. A direct experimental measurement of the frequency response between the x actuation signal and the in-plane crosstalk to the y-axis was not possible due to the measurement probe inaccessibility; however, the imaging results presented later show that the y cross talk is negligible.

C. Thermomechanical Coupling

Passing an electric current through the coil of the actuator generates heat. This effect is known as Joule or ohmic heating and is inevitable in electromagnetic actuators. According to Joule's first law, the power dissipated increases proportionally with the electrical resistance of the coil and with square of the current passed through the coil, i.e.,

$$P = I^2 R. \tag{9}$$

For example, with current $I = 1$ A and electrical resistance $R = 5\ \Omega$, the dissipated power will be approximately $P = 5$ W. Hence, it is imperative that a sufficient thermal isolation is provided which will prevent heating of the scanner body and its unwanted thermal expansion.

In the short-range scanner, the effect of the actuator ohmic heating on the position of the scan table is significantly decreased due to the mechanical and thermal decoupling of the actuator subassembly and the scan table. Owing to the small-section connection rod, the scan table is thermally isolated from the actuator subassembly. The actuator subassembly also has a strong heat conduction pathway to the main body of the scanner.

The coil heating was investigated experimentally by mapping the temperature distribution of the scanner using an infrared camera (FLIR SC5000) while the scanner is being actuated at its full scan range (6 μm, corresponding current 0.8 A). At the same time, point-based temperature measurements on the actuator subassembly and on the scan table were acquired using a calibrated thermometer (Fluke 54-2). The temperature profiles recorded and the corresponding time lapse image from the thermal camera are shown in Fig. 10. The measurements clearly show that the scan table remains relatively cool in spite of a continuous operation of the scanner over 150 s. Whereas the actuator subassembly heats up by approximately 10 °C due to the ohmic heating of the actuator coil, the increase of the scan table temperature is negligible over a short period time and does not exceed 2 °C over 150 s. The resulting thermal expansion of the scan table in the transient period is approximately 600 nm/degree for the scan axis and 200 nm/degree for the out-of-plane axis, relative to the temperature of the actuator subassembly. For scan operations with a short duration, or scan operations performed in the steady-state period, the disturbance caused by the ohmic heating is significantly smaller; typically, the displacement fluctuations are below 100 nm and owing to their low bandwidth, can be readily compensated by means of feedback control.

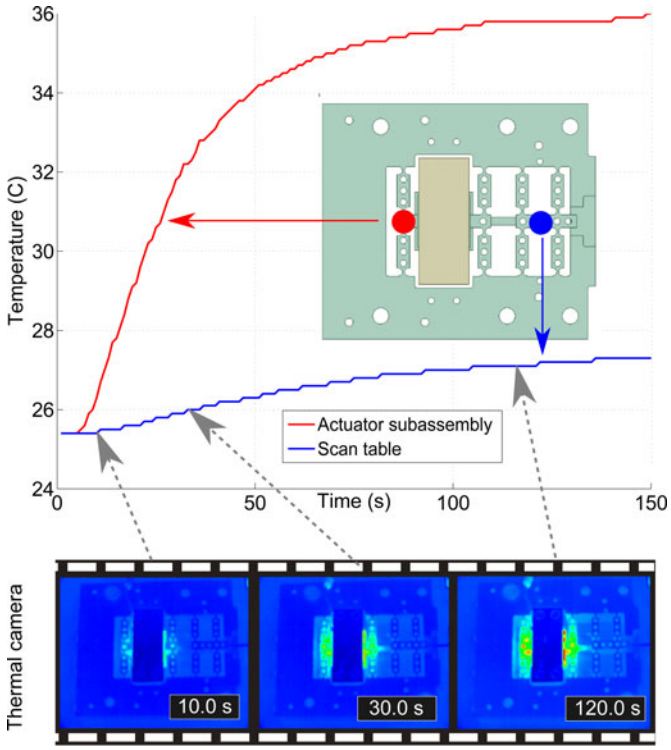

Fig. 10. Temperature distribution in the short-range scanner obtained by using an infrared camera and calibrated temperature measurements using contact sensors positioned on the actuator subassembly and on the scan table, respectively. In the thermal camera image, the bright green color corresponds to a temperature increase of approximately 10 °C with respect to the ambient room temperature (blue).

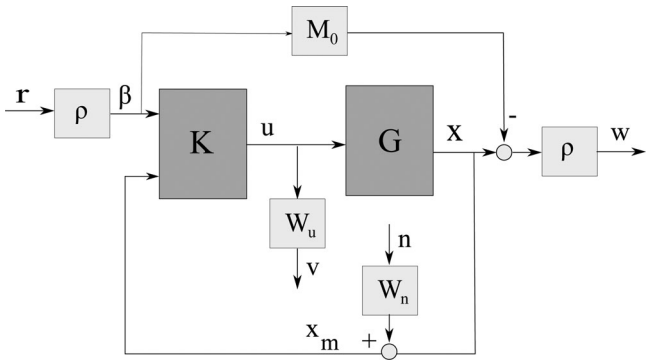

Fig. 11. Control design architecture for a two-degree-of-freedom robust controller with direct shaping of the noise sensitivity transfer function.

IV. Feedback Control

To achieve high positioning accuracy at high speeds, a feedback controller is designed to control the motion of the short-range scanner based on the position information from the GMR sensor. A robust control design procedure for a two-degree-of-freedom feedback controller is used in which the noise sensitivity of the feedback loop is directly shaped. The procedure combines the noise sensitivity shaping approach [15] with the robust performance design of [36] and is detailed in [32]. A schematic of the control design architecture is shown in Fig. 11.

For the purposes of the controller design, the dynamics of the short-range scanner were approximated with a second-order transfer function

$$G(s) = g \cdot \frac{\omega_n^2}{s^2 + 2\xi\omega_n + \omega_n^2}. \tag{10}$$

The damping ratio ξ and the natural frequency ω_n can be inferred from the mass-spring damper model introduced in Section II-C. Namely, the damping ratio is

$$\xi = \frac{c_a + c_s}{2\sqrt{(k_a + k_s)(m_a + m_s)}} \tag{11}$$

and the resonant frequency is

$$\omega_n = \frac{1}{2\pi}\sqrt{\frac{k_a + k_s}{m_a + m_s}}. \tag{12}$$

With the model parameters introduced in Table I, the values used in the second-order model are $\xi = 0.005$ and $\omega_n = 1768$ Hz. As discussed in Section II-C, slight deviations in the actual resonant frequency and damping ratio can occur due to manufacturing uncertainties and the sample weight.

The model in (10) captures only the low-frequency dynamics of the scanner and the first mechanical resonant mode at approximately 1.7 kHz. To keep the control design simple, the remaining resonant modes were omitted in the model and the resulting feedback loop was additionally shaped by a Butterworth band-stop filter centered at 10 kHz. The requirements on low sensitivity to the measurement noise, n, were reflected by choosing W_n as a second-order transfer function with band-stop characteristics in the frequency range from 500 Hz to 7 kHz. The limitations on control effort, u, were expressed by choosing W_u as a first-order low-pass filter with corner frequency of 10 kHz. In the process of control design, the targeted closed-loop transfer function M_0 between the reference, r, and the scanner position, x, and the scalar parameter ρ were chosen such that a desired tradeoff between robustness and performance was obtained. We refer the interested reader to [32] for more details on the control design.

The resulting controller has two degrees of freedom and consists of a prefilter component and a feedback component. The prefilter component is primarily responsible for matching the low-frequency gain and partly compensates for the lightly damped pole at approximately 1.7 kHz. The feedback component has a very low gain at low frequencies and its control effort is focused into the frequency range of 1 to 7 kHz. This is important for achieving the required closed-loop bandwidth and is in agreement with the limitations imposed by W_n. By design, there is no integral part in the controller; this is possible due to the linearity of the scanner. If needed, the integral part could be added by preshaping of the plant model prior to the control design.

The controller was discretized by using Tustin's method with sampling time of 20 μs and implemented in a digital signal processor. Fig. 12 compares the experimental open-loop response of the plant with the experimental closed-loop response. The closed-loop response is flat with bandwidth of 1.5 kHz which is important for tracking the broadband reference signals which arise in raster-based SPM. To evaluate the effect of the measurement noise which enters the feedback loop and affects the

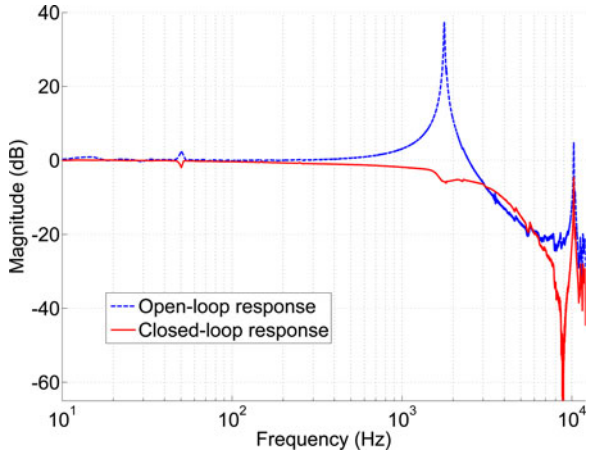

Fig. 12. Comparison of the open-looop and closed-loop transfer function of the scanner. The closed-loop frequency response is obtained using a two-degree of freedom noise-resilient feedback control design with approximately 40 pm projected measurement noise.

control action, we have used experimentally acquired noise measurements from the GMR sensor and computed the motion projected by the feedback loop to the output of the plant. It can be shown that the controller is sensitive to the measurement noise only in the frequency region of the resonant peak where feedback control is essential. Therefore, the standard deviation of the positioning error induced by the measurement noise in this feedback loop amounts to remarkable 0.04 nm. Note that this is the positioning error arising from measurement noise alone and that there might be other sources of positioning error such as the actuator and amplifier noise.

For a good overall performance, it is essential that all three axes of the large-range positioner are under feedback control. To that end, we used the standard Physik Instrumente PI-E612.C0 control box with analog integral controllers which use the built-in capacitive position sensors of the PI-517 stage. The controllers were tuned to approximately 20-Hz bandwidth which was sufficient for the low-bandwidth large-range scan operation. The cross-coupling between the large-range scanner and the short-range scanner was experimentally measured to be below -30 dB and did not require additional active compensation.

V. AFM Experiments

This section presents experiments in which the dual-stage nanopositioning system is used for imaging in a custom-designed high-speed AFM setup. The imaging experiments are based on the dual-stage raster scanning process. In this process, the sample is traversed back and forth in the x-axis by driving the short-range scanner with a high-frequency triangular waveform. The y-axis of the large-range scanner shifts the sample continuously in the direction orthogonal to the fast scan motion while the x-axis of the large-range scanner provides a dc offset to the fast scan motion. The z-axis of the large-range scanner is used to engage the cantilever with the sample surface during the imaging process.

Two experiments are presented: in the first experiment, the dual-stage system is used for high-speed short-range imaging with frame rates of more than 1 frame/s. In the second experiment, a comparably large sample area is decomposed into an array of small-range images and assembled into a single high-resolution image. In both experiments, the short-range and large-range scanner are under feedback control as described in Section IV. To allow for high precision tracking, the actuation frequencies are chosen such that at least the first three harmonics of the actuation signal are within the closed-loop bandwidth. Alternatively, scan trajectories with a more intricate shape could be used [37]–[39].

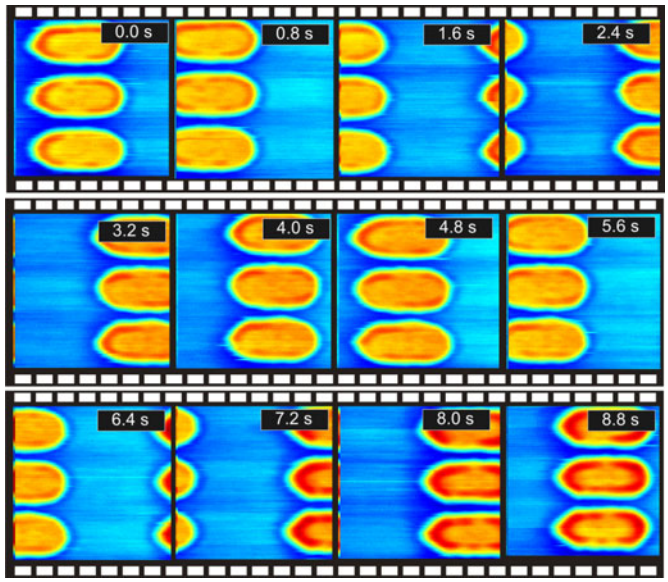

Fig. 13. Time-lapse sequence of high-resolution AFM topography estimates obtained in real-time by repeatedly shifting the sample along the x scan direction and imaging the sample with 1.25 frames/s. The scan range is 2×2 μm, the topographic height of the nanopatterns is approximately 100 nm.

In the imaging process, we used cantilevers with thermoelectric sensing capability [40], [41] and operated them in constant-height mode. The samples consist of a silicon surface with lithographic patterns of different dimensions; for each experiment, a different sample was used.

A. High-Frame-Rate Imaging

In the first experiment, the short-range scanner was actuated with a triangular waveform reference signal of frequency 250 Hz. The scan range was 2 μm $\times$ 2 μm, with spatial resolution 3 nm in the x-scan direction and 10 nm in the y-scan direction. Hence, a single frame consists of 655×200 pixels, and its imaging is completed in 0.8 s, yielding a frame rate of more than 1 frame/s. With this frame rate, interactive AFM imaging can be performed, in which high-quality AFM images are obtained on-the-fly.

During the experiment, the sample under investigation was examined along the x-scan direction. First, an AFM image was obtained at a given sample location, and subsequently, the position of the sample relative to the probe was shifted along the x-scan direction by using the large-range scanner. Fig. 13 shows time-lapse video images that were obtained during the experiment in which twelve images with a spacing of 400 nm were

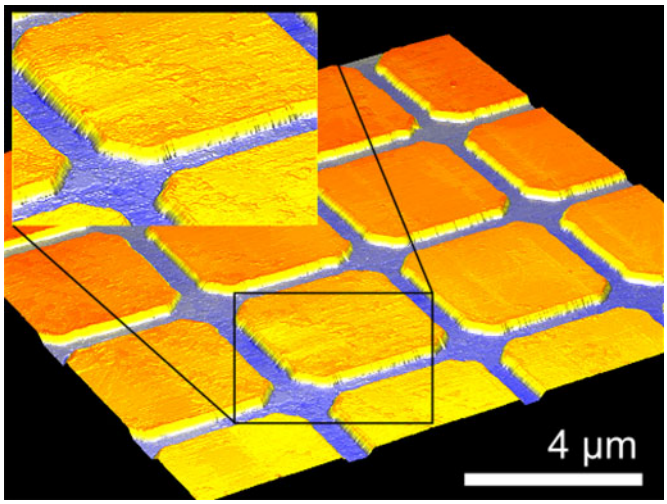

Fig. 14. Three-dimensional topography reconstruction of the lithographically patterned silicon surface. The image is based on the combined data from an array of 64 subimages acquired by the dual-stage nanopositioning system.

taken. Owing to the high-speed capabilities of the short-range scanner, real-time imaging of the sample was possible while the large-range scanner enabled large-range navigation over the sample surface.

B. Large-Range Imaging

In the second experiment, the imaged area of 16 μm $\times$ 16 μm was divided into 64 regular subregions of 2μm $\times$2μm which were imaged separately and patched together to form the resulting image. Each of the subframes was acquired in approximately 1.8 s by driving the short-range scanner with a triangular waveform of 113 Hz frequency, with the whole image being completed in approximately 2 min. The spatial resolution is 10 nm. Owing to the excellent mechanical properties of the short-range scanner, precise calibration of the sensors and the use of feedback control, the subframes are almost perfectly aligned and constitute a high-resolution, high-quality image of more than 2.5 million pixels. The 3-D topography reconstruction based on the combined image data is shown in Fig. 14.

VI. Conclusion

We presented a dual-stage approach to high-speed nanopositioning in which the conventional design tradeoffs between the scanner speed, range, and closed-loop resolution are addressed by combining a low-speed, large-range scanner with a high-speed, short-range scanner. We presented the design, finite-element simulations, modeling, and experimental characterization of an electromagnetically actuated short-range scanner. Using a magnetoresistance-based sensor and a tailored noise-resilient feedback control design, we showed that the scanner can be operated in closed loop with a positioning resolution of 0.04 nm. With the fast axis closed-loop bandwidth of 1.5 kHz the dual-stage system designed in this paper was used in a custom-built atomic force microscope to image an area of 2 $\times$ 2 μm with resolution of 655 $\times$ 200 pixels at a scan rate of 1.25 frames/s; using the same system, a 2.5 megapixel image of an area of 16 $\times$ 16 μm was obtained in approximately 2 min.

Acknowledgment

The authors would like to thank U. Egger for his assistance with the electronic hardware used in the experiments and H. Wolf for providing the sample. They would also like to thank G. Signorello for his help with the characterization of the sample and C. Bolliger for her assistance with the preparation of the manuscript. Special thanks go to H. Pozidis and E. Eleftheriou for their support of this study.

References

[1] E. Eleftheriou, T. Antonakopoulos, G. Binnig, G. Cherubini, M. Despont, A. Dholakia, U. Durig, M. Lantz, H. Pozidis, H. Rothuizen, and P. Vettiger, "Millipede—A MEMS-based scanning-probe data-storage system," *IEEE Trans. Magn.*, vol. 39, no. 2, pp. 938–945, Mar. 2003.

[2] R. A. Oliver, "Advances in AFM for the electrical characterization of semiconductors," *Rep. Progr. Phys.*, vol. 71, no. 7, p. 076501, 2008.

[3] T. Ando, T. Uchihashi, and T. Fukuma, "High-speed atomic force microscopy for nano-visualization of dynamic biomolecular processes," *Prog. Surf. Sci.*, vol. 83, pp. 337–437, 2008.

[4] S. M. Salapaka and M. V. Salapaka, "Scanning probe microscopy," *IEEE Control Syst. Mag.*, vol. 28, no. 2, pp. 65–83, 2008.

[5] S. Devasia, E. Eleftheriou, and S. O. R. Moheimani, "A survey of control issues in nanopositioning," *IEEE Trans. Control Syst. Technol.*, vol. 15, no. 5, pp. 802–823, Sep. 2007.

[6] G. Binnig and D. Smith, "Single-tube three-dimensional scanner for scanning tunneling microscopy," *Rev. Sci. Instrum.*, vol. 57, no. 8, pp. 1688–1689, 1986.

[7] J. Shim and D. Gweon, "Piezo-driven metrological multiaxis nanopositioner," *Rev. Sci. Instrum.*, vol. 72, pp. 4183–4187, 2001.

[8] S. Salapaka, A. Sebastian, J. Cleveland, and M. Salapaka, "High bandwidth nano-positioner: A robust control approach," *Rev. Sci. Instrum.*, vol. 73, pp. 3232–3241, 2002.

[9] G. Schitter and A. Stemmer, "Identification and open-loop tracking control of a piezoelectric tube scanner for high-speed scanning-probe microscopy," *IEEE Trans. Control Syst. Technol.*, vol. 12, no. 3, pp. 449–454, May 2004.

[10] G. Schitter, K. J. Astrom, B. E. DeMartini, P. J. Thurner, K. L. Turner, and P. K. Hansma, "Design and modeling of a high-speed AFM-Scanner," *IEEE Trans. Control Syst. Technol.*, vol. 15, no. 5, pp. 906–915, Sep. 2007.

[11] K. Leang and A. Fleming, "High-speed serial-kinematic SPM scanner: Design and drive considerations," *Asian J. Control*, vol. 11, no. 2, pp. 144–153, 2009.

[12] B. J. Kenton and K. K. Leang, "Design and control of a three-axis serial-kinematic high-bandwidth nanopositioner," *IEEE/ASME Trans. Mechatronics*, vol. 17, no. 2, pp. 356–369, Apr. 2012.

[13] V. Kartik, A. Sebastian, T. Tuma, A. Pantazi, H. Pozidis, and D. Sahoo, "High-bandwidth nanopositioner with magnetoresistance based position sensing," *Mechatronics*, vol. 22, no. 3, pp. 295–301, 2011.

[14] S. O. R. Moheimani and B. J. G. Vautier, "Resonant control of structural vibration using charge-driven piezoelectric actuators," *IEEE Trans. Control Syst. Technol.*, vol. 13, no. 6, pp. 1021–1035, Nov. 2005.

[15] A. Sebastian, A. Pantazi, S. O. R. Moheimani, H. Pozidis, and E. Eleftheriou, "Achieving subnanometer precision in a MEMS-based storage device during self-servo write process," *IEEE Trans. Nanotechnol.*, vol. 7, no. 5, pp. 586–595, Sep. 2008.

[16] A. Sebastian and S. O. R. Moheimani, "Signal transformation approach to fast nanopositioning," *Rev. Sci. Instrum.*, vol. 80, no. 7, pp. 076 101-1–076 101-3, 2009.

[17] T. Tuma, A. Sebastian, W. Häberle, J. Lygeros, and A. Pantazi, "Impulsive control for fast nanopositioning," *Nanotechnology*, vol. 22, p. 135501, 2011.

[18] D. Croft, G. Shed, and S. Devasia, "Creep, hysteresis, and vibration compensation for piezoactuators: Atomic force microscopy application," *J. Dyn. Syst., Meas., Control*, vol. 123, no. 1, pp. 35–43, 2001.

[19] B. Chen, T. Lee, K. Peng, and V. Venkataramanan, *Hard Disk Drive Servo Systems*. New York, NY, USA: Springer-Verlag, 2010.
[20] M. A. Lantz, H. E. Rothuizen, U. Drechsler, W. Haeberle, and M. Despont, "A vibration resistant nanopositioner for mobile parallel-probe storage applications," *J. Microelectromech. Syst.*, vol. 16, no. 1, pp. 130–139, 2007.
[21] A. Pantazi, A. Sebastian, T. A. Antonakopoulos, P. Baechtold, A. R. Bonaccio, J. Bonan, G. Cherubini, M. Despont, R. A. DiPietro, U. Drechsler, U. Duerig, B. Gotsmann, W. Haeberle, C. Hagleitner, J. L. Hedrick, D. Jubin, A. Knoll, M. A. Lantz, J. Pentarakis, H. Pozidis, R. C. Pratt, H. Rothuizen, R. Stutz, M. Varsamou, D. Wiesmann, and E. Eleftheriou, "Probe-based ultrahigh-density storage technology," *IBM J. Res. Develop.*, vol. 52, no. 4.5, pp. 493–511, 2008.
[22] G. Cherubini, R. Cideciyan, L. Dellmann, E. Eleftheriou, W. Haeberle, J. Jelitto, V. Kartik, M. Lantz, S. Ölcer, A. Pantazi, H. E. Rothuizen, D. Berman, W. Imaino, P.O. Jubert, G. McClelland, P. V. Koeppe, K. Tsuruta, T. Harasawa, Y. Murata, A. Musha, H. Noguchi, H. Ohtsu, O. Shimizu, and R. Suzuki, "29.5-GB/in2 recording areal density on barium ferrite tape," *IEEE Trans. Magn.*, vol. 47, no. 1, pp. 137–147, Jan. 2011.
[23] H. Butler, "Position control in lithographic equipment [applications of control]," *IEEE Control Syst. Mag.*, vol. 31, no. 5, pp. 28–47, Oct. 2011.
[24] S. G. Stan, *The CD-ROM Drive: A Brief System Description*. Norwell, MA, USA: Kluwer, 1998.
[25] M. Kobayashi and R. Horowitz, "Track seek control for hard disk dual-stage servo systems," *IEEE Trans. Magn.*, vol. 37, no. 2, pp. 949–954, Mar. 2001.
[26] S. Kwon, W. K. Chung, and Y. Youm, "On the coarse/fine dual-stage manipulators with robust perturbation compensator," in *Proc. IEEE Int. Conf. Robot. Autom.*, 2001, vol. 1, pp. 121–126.
[27] J. E. McInroy and S. S. Aphale, "Optimal filters from task velocities to joint velocities including both position and velocity limits," in *Proc. 42nd IEEE Conf. Decis. Control*, 2003, vol. 6, pp. 5885–5890.
[28] Q. Xu, "Design and development of a flexure-based dual-stage nanopositioning system with minimum interference behavior," *IEEE Trans. Autom. Sci. Eng.*, vol. 9, no. 3, pp. 554–563, Jul. 2012.
[29] G. Schitter, W. F. Rijkee, and N. Phan, "Dual actuation for high-bandwidth nanopositioning," in *Proc. IEEE Conf. Decis. Control*, 2008, pp. 5176–5181.
[30] S. Kuiper and G. Schitter, "Model-based feedback controller design for dual actuated atomic force microscopy," *Mechatronics*, vol. 22, no. 3, pp. 327–337, 2012.
[31] S. Andersson, "Curve tracking for rapid imaging in AFM," *IEEE Trans. Nanobiosci.*, vol. 6, no. 4, pp. 354–361, Dec. 2007.
[32] T. Tuma, W. Haeberle, H. Rothuizen, J. Lygeros, A. Pantazi, and A. Sebastian, "A dual-stage nanopositioning approach to high-speed scanning probe microscopy," in *Proc. 2012 Conf. Decis. Control*, 2012, pp. 5079–5084.
[33] T. Tuma, W. Haeberle, H. Rothuizen, J. Lygeros, A. Pantazi, and A. Sebastian, "A high-speed electromagnetically-actuated sanner for dual-stage nanopositioning," in *Proc. 6th IFAC Symp. Mechatron. Syst.*, 2013, pp. 125–130.
[34] R. Yang, M. Jouaneh, and R. Schweizer, "Design and characterization of a low-profile micropositioning stage," *Precis. Eng.*, vol. 18, no. 1, pp. 20–29, 1996.
[35] S. Wolf, D. Awschalom, R. Buhrman, J. Daughton, S. Von Molnar, M. Roukes, A. Chtchelkanova, and D. Treger, "Spintronics: A spin-based electronics vision for the future," *Science*, vol. 294, no. 5546, pp. 1488–1495, 2001.
[36] D. Limebeer, E. Kasenally, and J. Perkins, "On the design of robust two degree of freedom controllers," *Automatica*, vol. 29, no. 1, pp. 157–168, 1993.
[37] A. Fleming and A. Wills, "Optimal periodic trajectories for band-limited systems," *IEEE Trans. Control Syst. Technol.*, vol. 17, no. 3, pp. 552–562, May 2009.
[38] T. Tuma, J. Lygeros, A. Sebastian, and A. Pantazi, "Optimal scan trajectories for high speed scanning probe microscopy," in *Proc. 2012 Amer. Control Conf.*, 2012, pp. 3791–3796.
[39] T. Tuma, J. Lygeros, V. Kartik, A. Sebastian, and A. Pantazi, "High-speed multiresolution scanning probe microscopy based on Lissajous scan trajectories," *Nanotechnology*, vol. 23, p. 185501, 2012.
[40] W. P. King, T. W. Kenny, K. E. Goodson, G. Cross, M. Despont, U. Dürig, H. Rothuizen, G. Binnig, and P. Vettiger, "Atomic force microscope cantilevers for combined thermomechanical data writing and reading," *Appl. Phys. Lett.*, vol. 78, pp. 1300–1302, 2001.
[41] A. Sebastian and D. Wiesmann, "Modeling and experimental identification of silicon microheater dynamics: A systems approach," *J. Microelectromech. Syst.*, vol. 17, no. 4, pp. 911–920, 2008.

Tomas Tuma (M'09) studied computer science in the Department of Mathematics and Physics, Charles University, Prague, Czech Republic, where he received the Bachelor's and Master's degrees (both *summa cum laude*) in 2006 and 2009, respectively. He is currently working toward the Ph.D. degree in control engineering in the Automatic Control Laboratory, Swiss Federal Institute of Technology, Zurich, Switzerland.

Since 2009, he has been with IBM Research—Zurich, Rueschlikon, Switzerland, where he has been working on novel concepts for high-speed position control on the nanometer scale. His research interests include nanopositioning, nanoscale sensing, and scanning probe technologies.

Mr. Tuma was a winner of the IBM Great Minds program in 2008. In 2013, he received the "Student Best Paper Award" at the 6th IFAC Symposium on Mechatronics, held in Hangzhou, China.

Walter Haeberle joined the IBM Semiconductor Plant in Sindelfingen, Germany, and later graduated with the equivalent of a Master's degree in physical engineering from a joint vocational education and training program of Kerschensteiner College in Stuttgart, Germany, and the IBM Sindelfingen plant.

He is a Senior Development Engineer in the Storage Technologies Department, IBM Research—Zurich, Rueschlikon, Switzerland. In 1987, he joined the IBM Physics Group of Prof. G. K. Binnig at the University of Munich, Germany, where he contributed to the development of atomic force microscopes (AFMs) for applications in liquid environment for investigating living cells. In 1995, he transferred to the IBM Zurich Research Laboratory, where he was responsible for prototyping a new low-cost AFM instrument with good price/performance, which was later commercialized by Seiko Instruments, Japan. Since 1997 he has been involved in various aspects of the probe-based data-storage project including basic micro-scanner design and first measurements with 32×32 lever array chip. In 2003, he spent a sabbatical year at Wayne State University in Detroit, MI, USA. Intensify research on heat transfer rates in biological samples using thermo mechanical lever technologies. Since 2006, he has been involved in tape drive research with a focus on the tape path, especially on actuator design and track-following servo.

Hugo Rothuizen (M'09) received the Ph. D. degreee in applied physics from the Swiss Federal Institute of Technology, Lausanne, Switzerland, in 1994, with a dissertation on selective-area epitaxial growth of III–V materials.

Since becoming a Research Staff Member at the IBM Zurich Research Laboratory, Rueschlikon, Switzerland, in 1996, he has subsequently been working on the patterning of nanometer-scale structures, on the modeling of micromechanical sensors and actuators for data storage applications, and on high-performance liquid cooling. He is currently involved in the modeling and development of transducers for magnetic tape drives.

John Lygeros (F'11) received the B.Eng. degree in electrical engineering, and the M.Sc. degree in systems control from Imperial College of Science Technology and Medicine, London, U.K., in 1990 and 1991, respectively, and the Ph.D. degree from the Department of Electrical Engineering and Computer Sciences, University of California, Berkeley, CA, USA.

He is a Professor of Computation and Control at the Swiss Federal Institute of Technology (ETH), Zurich, Switzerland and is currently serving as the Head of the Automatic Control Laboratory. During the period 1996–2000, he held a series of research appointments at the National Automated Highway Systems Consortium, Berkeley, CA, USA, the Laboratory for Computer Science, Massachusetts Institute of Technology, Cambridge, MA, USA, and the Department of Electrical Engineering and Computer Sciences, University of California. Between 2000 and 2003, he was a University Lecturer in the Department of Engineering, University of Cambridge, Cambridge, U.K., and a Fellow of Churchill College. Between 2003 and 2006, he was an Assistant Professor in the Department of Electrical and Computer Engineering, University of Patras, Patra, Greece. In July 2006, he joined the Automatic Control Laboratory at ETH Zurich, first as an Associate Professor, and since January 2010, he has been a Full Professor. His research interests include modeling, analysis, and control of hierarchical, hybrid, and stochastic systems, with applications to biochemical networks, automated highway systems, air traffic management, power grids, and camera networks.

Dr. Lygeros is a member of the Institution of Engineering and Technology, U.K., and the Technical Chamber of Greece.

Angeliki Pantazi (M'06) received the Diploma and Ph.D. degrees in electrical engineering and computer technology from the University of Patras, Patra, Greece, in 1996 and 2005, respectively.

She joined IBM Research Zurich, Switzerland, in 2002, as a Ph.D. student and became a Research Staff Member in 2006. Her current research interests include scanning-probe techniques with emphasis on high-speed nanopositioning, emerging memory concepts such as phase-change memory, and control technologies for magnetic tape drive systems.

She has published more than 60 papers and holds more than 20 patents.

Dr. Pantazi was a co-recipient of the 2009 IEEE Control Systems Technology Award for contributions to nanopositioning for MEMS-based storage and other applications, the 2009 IEEE Transactions on Control Systems Technology Outstanding Paper Award, and the 2011 IBM Pat Goldberg Memorial Best Paper Award.

Abu Sebastian (SM'11) received the B. E. (Hons.) degree in electrical and electronics engineering from BITS Pilani, Pilani, India, in 1998, and the M. S. and Ph. D. degrees in electrical engineering from Iowa State University, Ames, IA, USA, in 1999 and 2004, respectively.

Since 2006, he has been a Research Staff Member at the IBM Research Zurich laboratory, Rueschlikon, Switzerland. His research is focused on dynamics and control at the nanometer scale. His research interests include scanning probe technologies, enabling tools for nanotechnology such as nanopositioning and nanoscale sensing and emerging memory, and storage technologies.

Dr. Sebastian received the 2013 IFAC Mechatronic Systems Young Researcher Award, and was a co-recipient of the 2009 IEEE Control Systems Technology Award and the 2009 IEEE TRANSACTIONS ON CONTROL SYSTEMS TECHNOLOGY Outstanding Paper Award. He is a Vice Chair of the IFAC Technical Committee on Mechatronics and serves on the Editorial Board of the journal *Mechatronics*. He is a member of the American Physical Society.